RSC Advances

PAPER

View Article Online
View Journal | View Issue

Cite this: *RSC Adv.*, 2022, **12**, 18697

Investigation of structural, morphological, and transport properties of a multifunctional Li-ferrite compound

Ibtihel. Soudani, [a] Khawla. Ben Brahim, *[b] Abderrazek. Oueslati, [b] Houda. Slimi, [a] Abdelhedi. Aydi[a] and Kamel. Khirouni[c]

The development of multifunctional materials is an exceptional research area, which is aimed at enhancing the versatility of materials in various applications. In this context, the exceptional properties of ferrite materials have attracted the attention of researchers. For this reason, we synthesized $LiMn_{0.5}Fe_2O_4$ sintered at a temperature of 1100 °C. The X-ray powder diffraction analysis reveals the presence of one cubic phase with the $Fd\bar{3}m$ space group and confirms the spinel structure formation. Moreover, the elemental analysis by EDX reveals the homogeneous distribution of iron and manganese cations. Scanning electron microscopy shows that the grain size is of the order of 2.48 μm. Impedance spectroscopy was performed in the temperature and frequency ranges from 200 K to 380 K and 40 Hz to 10^6 Hz, respectively. The Nyquist plots revealed the presence of grains and grain boundary contributions. The semiconductor nature, obtained by the conductivity study, indicates that $LiMn_{0.5}Fe_2O_4$ is promising in optoelectronic applications. Dc conductivity is found to be thermally activated with an activation energy of 370 meV, 255 meV, and 199 meV for 200–270 K, 280–330 K, and 340–380 K regions, respectively. From the Jonscher power law, the correlated barrier hopping model (CBH) and non-overlapping small polaron tunneling (NSPT) prevailed in the conduction process. Besides, the temperature coefficient of resistivity (TCR) affirmed that $LiMn_{0.5}Fe_2O_4$ is a good candidate for detecting infrared radiations and infrared bolometric applications.

Received 30th April 2022
Accepted 8th June 2022

DOI: 10.1039/d2ra02757g

rsc.li/rsc-advances

1. Introduction

Many efforts have been focused during the last years on the preparation of ferrite materials, which has become the object of numerous experimental studies.[1–3] Spinel ferrites generally possess a cubic spinel structure with the formula AFe_2O_4, where A is usually a divalent metal for satisfying the current manufacturing demands. This structure presents the ideal stoichiometry of spinel ferrite, which fulfills the conditions of the cation/anion ratio of 3/4. However, the existing spinel materials that are far from this stoichiometry are the most known spinel ferrites, such as maghemite (g-Fe_2O_3).[4] This implies the presence of nonstoichiometric spinels depending on the overall cation/anion ratio. When the cation-to-anion ratio is lower than 3/4, hypostoichiometry is observed. Spinels show hyperstoichiometry when the ratio is higher than 3/4.

Significant findings and achievements have been attained for ferrite substances, especially lithium ferrites, which comprise an exciting class of materials having a non-stoichiometric spinel structure. For instance, Li–Co,[5] Li–Zn,[6,7] Li–Ti,[8] Li–Mg,[9] and Li–Ni (ref. 10 and 11) generally show excellent physicochemical properties. It is observed that there is a significant change in the properties of lithium ferrites by substitution of different metal cations. This fact motivated G. Aravind *et al.* to synthesize nickel-substituted lithium ferrites.[12] Ni-doped $Li_{0.5}Fe_{2.5}O_4$ show superparamagnetic behavior that makes it a good candidate for biomedical applications. Also, the magnetic investigation of $Li_{0.06}Fe_{2.94}O_4$ reveals that it may be suitable for magnetic hyperthermia (MHT) treatments in cancer applications.[13]

This category of materials belongs to soft materials that can be extensively used in computer memory chips, transformer cores rod antennas, microwave devices, medical diagnostics, magnetic resonance imaging, magnetic caloric refrigeration, and radiofrequency coil fabrication.[14–18] Besides, these substances have drawn a great deal of interest in modern technological applications in the telecommunication field, electronics engineering, electric vehicles, and memory storage

[a]*Laboratory of Multifunctional Materials and Applications (LaMMA), LR16ES18, Faculty of Sciences of Sfax, University of Sfax, BP 1171, 3000 Sfax, Tunisia*

[b]*Laboratory for Spectroscopic and Optical Characterization of Materials (LaSCOM), Faculty of Sciences, University of Sfax, B. P. 1171, 3000 Sfax, Tunisia. E-mail: benbrahimkhawla75@gmail.com*

[c]*Laboratory of Physics of Materials and Nanomaterials Applied to the Environment (LaPHYMNE), Faculty of Sciences, University of Gabès Cited Erriadh, 6079 Gabès, Tunisia*

devices.[19,20] It can be a good inductive component in an enormous diversity of electrical instruments, for instance impedance matching networks,[6] filters,[21] voltage-controlled rectifiers,[5] and low noise amplifiers.[22]

The distinguishable properties such as environmental benignity,[23] low eddy current values,[24] high electrical resistivity,[24] availability at low cost,[25] lightweight, and superior high-temperature performance can give it a considerable stature in future multifunctional application. Therewith, its efficacity can be improved by tuning the electrical resistivity and eddy current. This may explain the increasing scientific curiosity toward Li-ferrite materials.

Several synthetic approaches have been developed to prepare the nanoparticles of this eminent category of ferrites including sol–gel,[26] hydrothermal,[27] micro-emulsion technique,[5] auto-combustion,[28] and the solid-state reaction route (ceramic).[29] A majority of these synthesis methods are economically impracticable for large-scale production. However, the solid-state reaction has proven its effectiveness for several years due to its simplicity, high crystallinity, homogeneity of the product, and its low cost compared with other synthesis methods.

To date, the reports on Li–Mn-based ferrites are limited, despite it being suitable for the fabrication of cathode materials for Li-rechargeable batteries,[30] and it is used in the improvement of memory cores that merge low-temperature sensitivity with fast switching.[31]

In this context, we report a further study on $LiMn_{0.5}Fe_2O_4$ prepared by the solid-state reaction technique. This compound is a hyper stoichiometric spinel material with a cation/oxygen ratio higher than 3/4. After discussing its structure and morphological analysis, the electrical properties are investigated to thoroughly explain the transport phenomena by combining conductivity and impedance studies. The main objective of this work is not only to show an excellent material but also a large range of applications in the future.

2. Experimental details

2.1 Materials synthesis

In general, before the preparation of the material, a series of synthesis optimization were done separately for obtaining a sample sufficiently homogenous and well crystallized with expected and reasonable final properties. All reagents obtained from Sigma-Aldrich Li_2CO_3, MnO, and Fe_2O_3 were of analytical purity grade (99.9%, Sigma-Aldrich) and used without further purification. They were used for synthesizing $LiMn_{0.5}Fe_2O_4$. In the first stage, these precursors were carefully weighted in stoichiometric amounts. In the next step, the mixed powder was ground neatly in an agate mortar for 2 hours to reduce the size of the grain, and hereafter, the mixture was heated. Then, the resulting mixture was heated slowly to 850 °C. It was left at this temperature for 7 hours to activate the chemical reaction and to fix different elements to limit their volatilization. Also, the sample pellets of $LiMn_{0.5}Fe_2O_4$ were embedded in the calcined powder to avoid severe lithium evaporation during sintering.

Once the reaction was completed, the obtained powder was ground for 1 hour and pressed into a circular disc of 8 mm diameter and 1 mm thickness. To obtain a high-density ceramic with perfect crystallization, the pellet was sintered at 1100 °C for 2 hours in an electric muffle furnace and slowly cooled to room temperature. Finally, the pellet was ready to be characterized.

2.2 Characterization tools

The X-ray powder diffraction pattern of our ferrite was recorded at room temperature using a BRUKER diffractometer with copper anticathode (CuK_α radiation $\lambda = 1.5406$ Å) in the Bragg range from 10 to 90°. The morphological characterization was performed by a scanning electron microscope (SEM) in order to estimate the particle size. To investigate the chemical compositions, energy-dispersive X-ray (EDX) images and simple mapping were done.

The electrical properties of $LiMn_{0.5}Fe_2O_4$ were determined by impedance spectroscopy. Two proper thin layers of silver were put on each surface of the synthesized pellet through a circular mask by thermal evaporation. The pellet was placed in a cryostat from Janis Corporation, which allowed the temperature to be varied from 200 to 380 K. The conductance and impedance measurements were done using an Agilent 4294 A analyzer under vacuum over the explored frequency range from 40 Hz to 10^6 Hz.

3. Results and discussion

3.1 Structural study

The crystalline structure and the formed phase-purity of $LiMn_{0.5}Fe_2O_4$ were characterized through X-ray powder diffraction (XRD) measurement performed at room temperature. The refinement of the XRD pattern was performed by the Rietveld method using the Full PROF program.[32] Fig. 1 shows

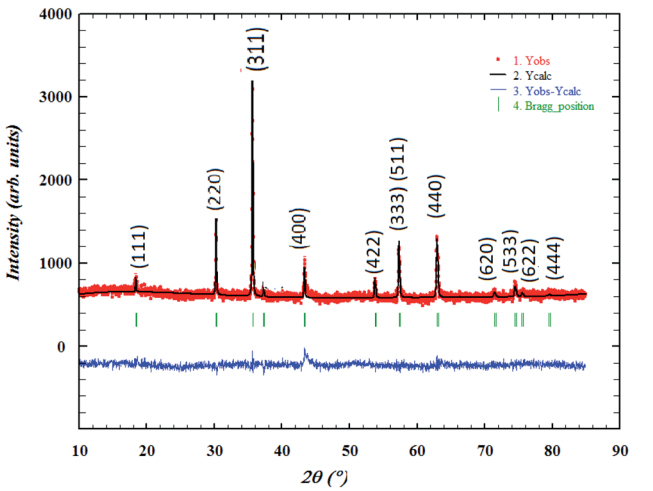

Fig. 1 Refined XRPD patterns of $LiMn_{0.5}Fe_2O_4$ at room temperature. The red dotted line stands for the experimental data. The calculated data are represented by a black continuous line. The curve in blue shows the difference between the experimental and calculated patterns. The vertical bars in green indicate the Bragg positions.

the observed, calculated, and difference diffraction patterns. All Bragg peaks are successfully indexed and satisfactorily modeled without any extra peaks related to hematite (Fe_2O_3) or any foreign impurity. This confirms the superior purity of the prepared sample. The diffraction results show that our compound is a cubic system with $Fd\bar{3}m$ space group (O_7^h point group), as expected for the ferrite structures, according to the JCPDS card no. 96-152-6193.

The strongest reflection comes from the (311) plane, which denotes the spinel phase formation.[33] All the Rietveld refinement parameters are reported in Table 1.

The weak value of the goodness fit parameter (χ^2) confirms the rigor of the refining and the precision of the fit. The crystal structure, projected in the (110) plan, of the compound, is schematically depicted in Fig. 2 using the Diamond software.

The average crystallite size (D_{sc}) shown in Table 1 is determined from the full width at half maximum using the classical Debye–Scherrer equation.[34]

$$\beta \cos \theta D_{sc} = K\lambda \quad (1)$$

where β is the half-width measured for the intense diffraction peak corresponding to the plane (hkl), θ is the diffraction Bragg angle for the most intense peak in radian, D_{sc} is the crystallite size, K is the shape factor of approximate value 0.9, and λ is the wavelength of the used X-ray. The crystallite size value of $LiMn_{0.5}Fe_2O_4$ is approximately 46 nm, which proves the nanometer size of our ferrite sample.

The link lengths between cations occupying the tetrahedral positions (A) and cations placed in the octahedral positions (B) (L_{A-A}, L_{B-B}, and L_{A-B}) depend only on the lattice parameter (a). They are calculated employing the equations of Standely.[34]

$$L_{A-A} = 0.25\left(a\sqrt{3}\right) \quad (2)$$

$$L_{B-B} = 0.125\left(a\sqrt{11}\right) \quad (3)$$

$$L_{A-B} = 0.25\left(a\sqrt{2}\right) \quad (4)$$

Table 1 Rietveld refinement parameters of $LiMn_{0.5}Fe_2O_4$

Formula	$LiMn_{0.5}Fe_2O_4$ at room temperature
Crystalline system	Cubic
Space group	$Fd\bar{3}m$
Lattice parameter (Å)	
$a = b = c$	8.343
$\alpha = \beta = \delta$ (°)	90
V (Å^3)	580.913
Reliability factors (%)	
R_p (%)/R_{wp} (%)/R_{exp} (%)	3.960/5.090/4
χ^2	1.620

The density ($\rho_{X\text{-ray}}$) is fixed, bearing in mind that a cubic spinel structure consists of a unit cell including eight molecules, according to the following formula.[34]

$$\rho_{X\text{-ray}} = \frac{8M}{a^3 N_A} \quad (5)$$

In this expression, M denotes the molecular weight of each compound of the studied spinel ferrite, a denotes the calculated lattice parameter determined from the XRD measurements, and N_A ($=6.023 \times 10^{23}$) represents Avogadro's number.

The bulk density of $LiMn_{0.5}Fe_2O_4$ is calculated using the following standard relation:[34]

$$\rho_{exp} = \frac{m}{\pi r^2 t} \quad (6)$$

where r is the radius, t is the thickness, and m is the mass of the sintered pellets. Besides, the porosity is evaluated by the difference between the experimental density (ρ_{exp}) and the density ($\rho_{X\text{-ray}}$) as follows.[34]

$$P(\%) = \left[1 - \frac{\rho_{exp}}{\rho_{X\text{-ray}}}\right] \times 100 \quad (7)$$

The specific surface area (S_a) is obtained from the following expression.[34]

$$S_a = \frac{6000}{D_{sc}\rho_{X\text{-ray}}} \quad (8)$$

where D_{sc} is the crystallite size in nm, which is deduced from the classical Debye Scherrer model, and $\rho_{X\text{-ray}}$ is the density of the particle in g cm^{-3}.

All details deduced from previous analyses are tabulated in Table 2.

The specific surface and porosity percentage have an important role in controlling the diverse properties of polycrystalline spinel ferrites. They exhibit that the particle size of the spinel is nearly homogeneous, uniformly distributed, and well agglomerated over the whole surface of the studied sample.[34]

3.2 Morphological study

Elemental analysis by EDX is used to characterize the chemical composition of the sample. It gives the qualitative and quantitative analysis of the elements present in the prepared compound. The spectrum obtained is shown in Fig. 3a. The characteristic peaks of the constituent elements, namely, manganese (Mn), iron (Fe), and oxygen (O), are demonstrated without any impurity. This is good evidence of the purity of the synthesized sample. On the other hand, the appearance of the carbon (C) signal can be ascribed to carbon tape on which the sintered pellet is mounted with a holder.[35] Nevertheless, the small atomic number (Z) of lithium element, which is less than the sensitivity of EDX to the element's atomic number, explains its invisibility in the spectrum.[30]

Fig. 3b shows the EDX mapping analysis of $LiMn_{0.5}Fe_2O_4$. The distribution of the elements is presented with different colors (Mn (royal blue), Fe (green), and O (red)).

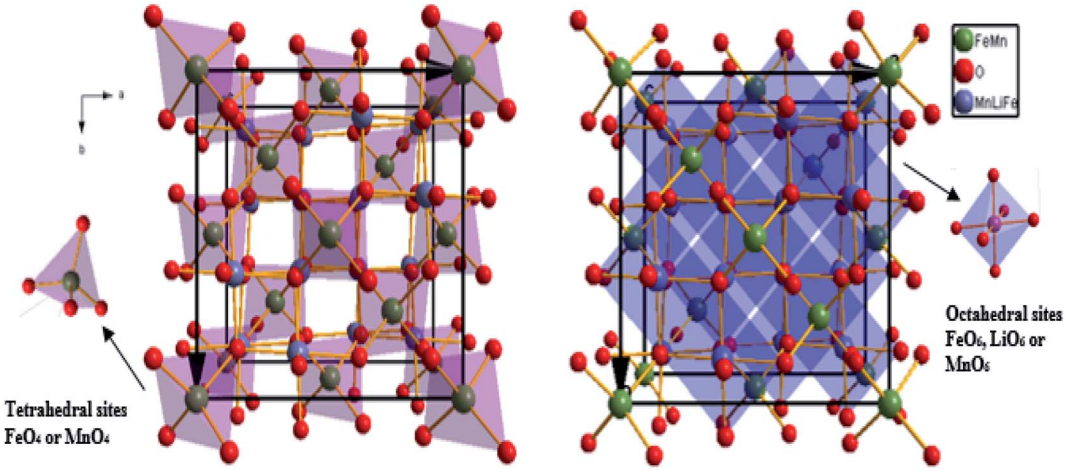

Fig. 2 Oxide lithium-manganese ferrite spinel representation, with stoichiometry $LiMn_{0.5}Fe_2O_4$, in the (110) plane. Tetrahedral sites of FeO_4 or MnO_4 are presented in red color and octahedral sites of FeO_6, LiO_6, or MnO_6 are presented in blue.

It highlights that all elements are approximately uniformly distributed at the micrometer scale in the sample. Small differences can be ascribed to the different crystallographic orientations.

The experimental and theoretical proportions of the constituents obtained as an atomic percentage are recorded in Table 3. The experimental weight and atomic percentages are in agreement with the expected theoretical values. This proves the success of the pathway for the synthesis of $LiMn_{0.5}Fe_2O_4$.

The EDX result indicates that the preparation denotes a homogeneous distribution of iron and manganese cations with high purity.

The micrograph displayed in Fig. 3a illustrates an interesting surface morphology of $LiMn_{0.5}Fe_2O_4$. Scanning electron microscopy reveals a high melting or accumulation microstructure with polygonal-shaped and polyhedron-shaped grains. The average grain size of the particles (D_{SEM}) is deduced by fitting the histogram (Fig. 3c) by employing the image analyzer software ImageJ. D_{SEM} is about 2.48 μm. This means that the grains have a polycrystalline structure, compared with the low crystallite size obtained from the XRD study.[36]

3.3 Electrical results

3.3.1 Impedance studies. Complex impedance spectroscopy is a widely used tool to evaluate the electrical characterization response of ferrite materials over a wide range of frequencies and temperatures. It is well known as the most powerful technique to examine the electric behavior and dynamics of ionic movement in the investigated material.[37] In fact, this tool is extremely useful in differentiating the transport characteristics and determining the contributions of different mechanisms in the conduction process.[38]

The Nyquist diagram of $LiMn_{0.5}Fe_2O_4$ at a chosen temperature is shown in Fig. 4a and b. These diagrams reveal a succession of semicircles that reflect the grain and grain boundary contributions. Two distinct behaviors are observed below (Fig. 5a) and after (Fig. 5b) 270 K.

Two semicircular arcs are observed in Fig. 4a for the temperature range of 200–270 K, which is related to the grain and the grain boundary effects. In order to extract the different electrical parameters, the experimental data are modeled as an equivalent circuit formed by a series of two parallel combinations. The first one consists of resistance (R_1) and a constant phase element (CPE_1), and the second one is composed of a parallel combination of resistance (R_2), capacitance (C_1), and a constant phase element (CPE_2) (Fig. 4a inset).

The impedance of CPE is given by[39]

$$Z_{CPE} = \frac{1}{Q(j\omega)^{\alpha}} \quad (9)$$

Table 2 X-ray parameters, X-ray density ($\rho_{X\text{-ray}}$), bulk density (ρ_{exp}), porosity (P), and specific surface area (S) of $LiMn_{0.5}Fe_2O_4$

Average crystallite size (nm)	D_{sc}	46
Average interionic bond distances between the cations' positions (Å)	$L_{A\text{–}A}$	3.61
	$L_{B\text{–}B}$	3.27
	$L_{A\text{–}B}$	2.95
Tetrahedral (A) site radii (Å)	r_A	0.62
Octahedral (B) site radii (Å)	r_B	0.64
Density (g cm^{-3})	$\rho_{X\text{-ray}}$	4.81
Bulk density (g cm^{-3})	ρ_{exp}	4.68
Porosity	P	3
Specific surface area (m^2 g^{-1})	S_a	27.11

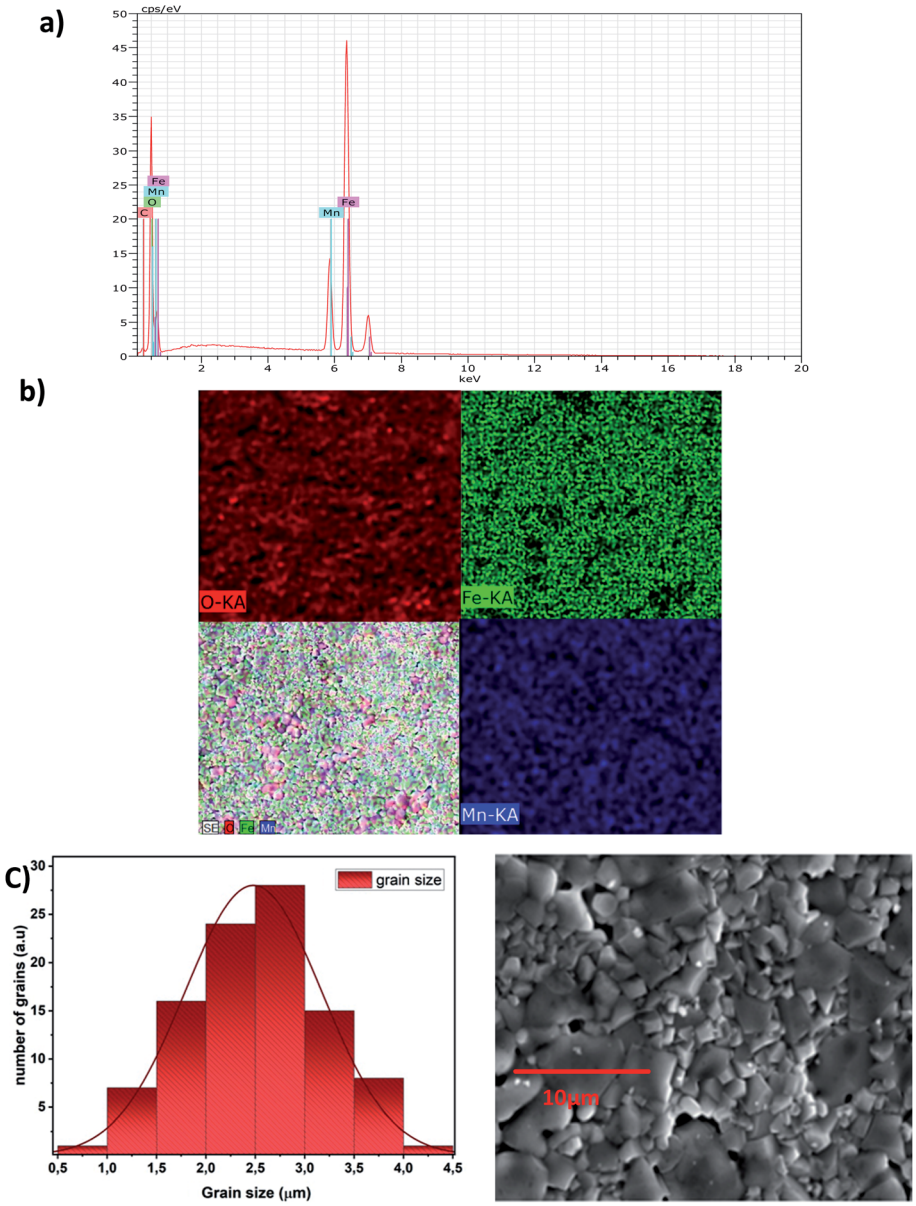

Fig. 3 EDX spectra of $LiMn_{0.5}Fe_2O_4$ (a), EDX mapping analysis of $LiMn_{0.5}Fe_2O_4$ (b), scanning electron microscopy images of $LiMn_{0.5}Fe_2O_4$ at scale of 10 μm, and distribution histogram of grains of $LiMn_{0.5}Fe_2O_4$ (c).

Table 3 The experimental proportions of the constituents obtained by EDS and the theoretical ones in $LiMn_{0.5}Fe_2O_4$

	Experimental values		Theoretical values	
Element	Weight (%)	Atom (%)	Weight (%)	Atom (%)
Carbon	1.66	4.17	—	
Oxygen	31.60	59.64	30.46	53.33
Manganese	12.08	6.64	15.69	6.66
Iron	54.66	29.55	53.17	26.66

which refers to the complex element. Here, ω is the angular frequency, Q is the proportional factor, and α describes the deviation of the line in the Nyquist plot from the vertical $0 < \alpha < 1$. At $\alpha = 1$, the constant phase element is an ideal capacitive element and at $\alpha = 0$, it indicates resistance. Q and α depend only on the temperature. We can deduce the real part (Z') and the imaginary part (Z'') of complex impedance, which are expressed by the following equations.[40]

$$Z' = \frac{R_1\left(1 + R_1Q_1\omega^{\alpha_1}\cos\left(\alpha_1\frac{\pi}{2}\right)\right)}{\left(1 + R_1Q_1\omega^{\alpha_1}\cos\left(\alpha_1\frac{\pi}{2}\right)\right)^2 + \left(R_1Q_1\omega^{\alpha_1}\sin\left(\alpha_1\frac{\pi}{2}\right)\right)^2} + \frac{R_2{}^{-1} + Q_2\omega^{\alpha_2}\cos\left(\alpha_2\frac{\pi}{2}\right)}{\left(R_2{}^{-1} + Q_2\omega^2\cos\left(\alpha_2\frac{\pi}{2}\right)\right)^2 + \left(c\omega + Q_2\omega^{\alpha_2}\sin\left(\alpha_2\frac{\pi}{2}\right)\right)^2} \quad (10)$$

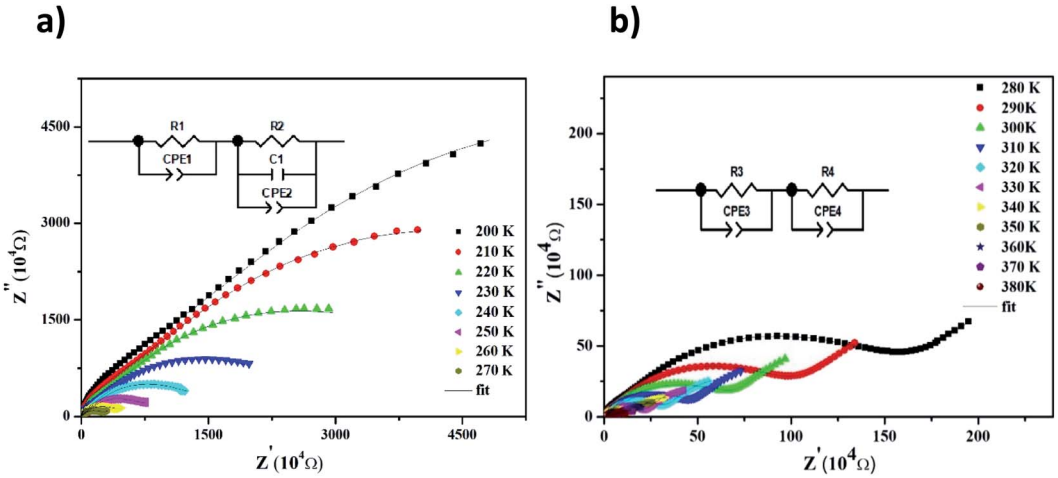

Fig. 4 Complex impedance spectra in the Nyquist plane with electrical equivalent circuit (inset), accompanied by theoretical data (solid lines) at 200–270 K (a) and 280–380 K (b).

$$Z'' = \frac{R_1^{\,2} Q_1 \omega^{\alpha_1} \sin\left(\alpha_1 \frac{\pi}{2}\right)}{\left(1 + R_1 Q_1 \omega^{\alpha_1} \cos\left(\alpha_1 \frac{\pi}{2}\right)\right)^2 + \left(R_1 Q_1 \omega^{\alpha_1} \sin\left(\alpha_1 \frac{\pi}{2}\right)\right)^2} + \frac{c\omega + Q_2 \omega^{\alpha_2} \sin\left(\alpha_2 \frac{\pi}{2}\right)}{\left(R_2^{-1} + Q_2 \omega^{\alpha_2} \cos\left(\alpha_2 \frac{\pi}{2}\right)\right)^2 + \left(c\omega + Q_2 \omega^{\alpha_2} \sin\left(\alpha_2 \frac{\pi}{2}\right)\right)^2} \quad (11)$$

From 280 K to 380 K, the compound can be modeled by an equivalent circuit model. It implies a serial association of grain resistance (R_3) associated in parallel with (CPE_3) and (R_4) resistance grain boundary associated in parallel with (CPE_4). The equivalent circuit is deposited, as shown in the inset of Fig. 4b. Based on this model, we can obtain the subsequent expressions:[41]

$$Z' = \frac{R_3\left(1 + R_3 Q_3 \omega^{\alpha_3} \cos\left(\alpha_3 \frac{\pi}{2}\right)\right)}{\left(1 + R_3 Q_3 \omega^{\alpha_3} \cos\left(\alpha_3 \frac{\pi}{2}\right)\right)^2 + \left(R_3 Q_3 \omega^{\alpha_3} \sin\left(\alpha_3 \frac{\pi}{2}\right)\right)^2} + \frac{R_4\left(1 + R_4 Q_4 \omega^{\alpha 4} \cos\left(\alpha_4 \frac{\pi}{2}\right)\right)}{\left(1 + R_4 Q_4 \omega^{\alpha_4} \cos\left(\alpha_4 \frac{\pi}{2}\right)\right)^2 + \left(R_4 Q_4 \omega^{\alpha_4} \sin\left(\alpha_4 \frac{\pi}{2}\right)\right)^2} \quad (12)$$

$$Z'' = \frac{R_3^{\,2} Q_3 \omega^{\alpha_3} \sin\left(\alpha_3 \frac{\pi}{2}\right)}{\left(1 + R_3 Q_3 \omega^{\alpha_3} \cos\left(\alpha_3 \frac{\pi}{2}\right)\right)^2 + \left(R_3 Q_3 \omega^{\alpha_3} \sin\left(\alpha_3 \frac{\pi}{2}\right)\right)^2} + \frac{R_4^{\,2} Q_4 \omega^{\alpha_4} \sin\left(\alpha_4 \frac{\pi}{2}\right)}{\left(1 + R_4 Q_4 \omega^{\alpha_4} \cos\left(\alpha_4 \frac{\pi}{2}\right)\right)^2 + \left(R_4 Q_4 \omega^{\alpha_4} \sin\left(\alpha_4 \frac{\pi}{2}\right)\right)^2} \quad (13)$$

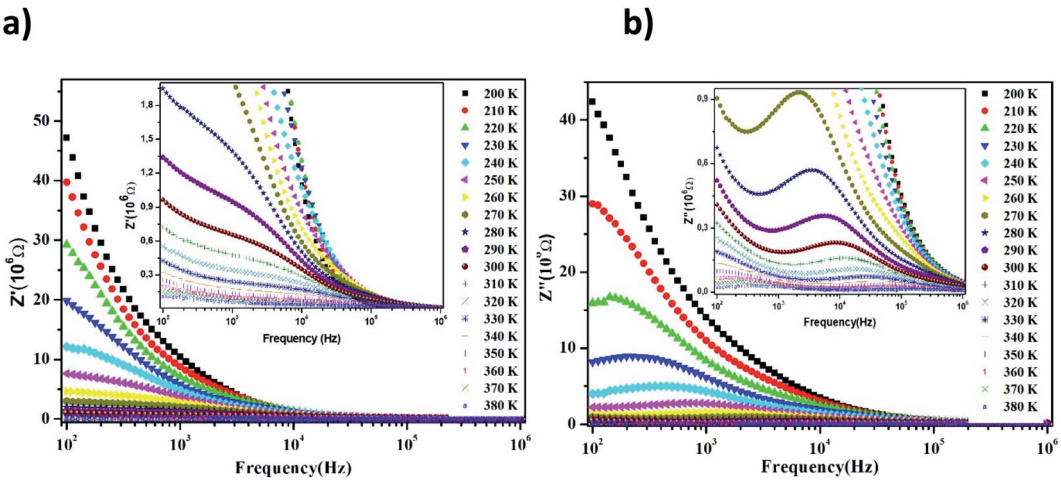

Fig. 5 Frequency evolution of the real part of the impedance plot of $LiMn_{0.5}Fe_2O_4$ at selected temperatures (a) and frequency evolution of the imaginary part of the impedance plot of $LiMn_{0.5}Fe_2O_4$ at selected temperatures (b).

The real and imaginary parts of impedance plots at several temperatures show an ordinary behavior, observed in many materials,[42,43] as depicted in Fig. 5. We can observe in Fig. 5a that with a further increase in frequency, the real impedance part comes down to a particular frequency depending on the temperature. Then, all curves of the value Z' merge into a single line at a higher frequency side for all temperatures. This can be clarified by the release of space charges caused by the reduction of barriers in the investigated material.[44] In fact, a decrease in the real part of impedance Z' at the lower frequency limit region can be accounted by the NTCR (negative temperature coefficient of resistance) nature of the material according to other previous works.[45,46] However, other researchers have explained the decreasing trend of Z' at the lower frequency limit region by the increase in the AC conductivity and the decrease in the trapped charge density guide for an increase in the charge carrier mobility.[47] All these suggestions will be discussed in the parts that follow.

Fig. 5b displays the behavior of Z'', the imaginary part of impedance, with the variation in the frequency at a wide range of temperatures (200–380 K). The value of Z'' increases gradually with the frequency as the temperature increases, until it reaches a maximum peak Z_{max}''. Then, this magnitude decreases. These observations reflect the existence of the electrical relaxation phenomena and describe its type and its strength in our material.[48,49]

For higher frequencies and for all temperatures, the imaginary part of Z'' is merged. It can be explained by an accumulation of the space charge effect in the material, as reported in the preceding investigation.[50,51] Here, in Fig. 5b, we observe that when the temperature increases, the relaxation peaks shift toward higher frequencies. This behavior indicates an increase in the mobility of the hopping charge carrier, which reveals the drop of the resistive properties in the bulk of the material.[52] Also, it indicates the presence of a thermally-activated relaxation process and allows us to estimate its activation energy value in $LiMn_{0.5}Fe_2O_4$.

Afterward, we plotted the variation of $\ln(f_{max})$ *vs.* $1000/T$ in Fig. 6, where f_{max} corresponds to the relaxation frequency at each maximum of Z''. The determined curve can be described using Arrhenius law[53]

$$f_{max} = f_0 \exp\left(-\frac{E_a}{k_B T}\right) \quad (14)$$

where E_a is the activation energy, f_0 is the pre-exponential factor, k_B is Boltzmann's constant, and T is the measured temperature. We extracted three values of activation energy from the straight-line region of the Arrhenius plot (Fig. 6), which are 361 meV for the first region, 280 meV for the second region, and 192 meV for the third region. The activation energy increases when the temperature increases. Finally, all these results suggest that $LiMn_{0.5}Fe_2O_4$ can be suitable for many technological applications such as weak temperature cofired ceramics applications, microwave applications, and fuel cells.[6]

The existence of multivalent cations such as manganese (Mn^{3+}, Mn^{2+}), iron (Fe^{3+}, Fe^{2+}), and their displacement between the A and B sites of the studied sample $LiMn_{0.5}Fe_2O_4$ certainly enhanced the electrical proprieties.[30] The crystal lattice always tends toward a stable configuration. Therefore, certain ions are obligated to move according to the other new ion position. This jumping ion activates the electron–phonon interaction and the lattice vibration and plays a noteworthy role in the control of the conduction mechanism as a function of temperature.[7]

All this will be supported through the study of the conductive behavior, which will be discussed in the following part.

3.3.2 Conductivity studies. Conductivity measurement (σ_T) response is a significant factor that gives us important information about the conduction process in the materials. In this way, the variation of conductivity of the studied compound is illustrated in Fig. 7. From these curves, we can detect two distinct regions.

At the lower frequencies (10^2 –10^4 Hz), the conductivity spectra have nearly constant values (σ_{dc}) because the random distribution of the charges carriers gives rise to frequency-independent conductivity.[54] It is clear that dc conductivity is thermally activated, which can display the semiconductor

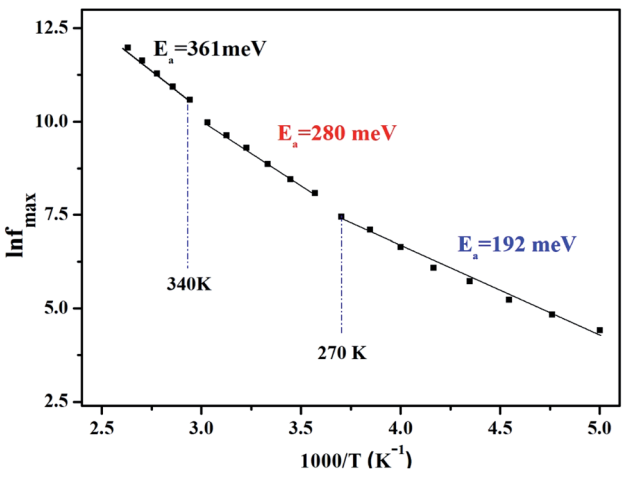

Fig. 6 Variation of ln (f_{max}) *vs.* $1000/T$.

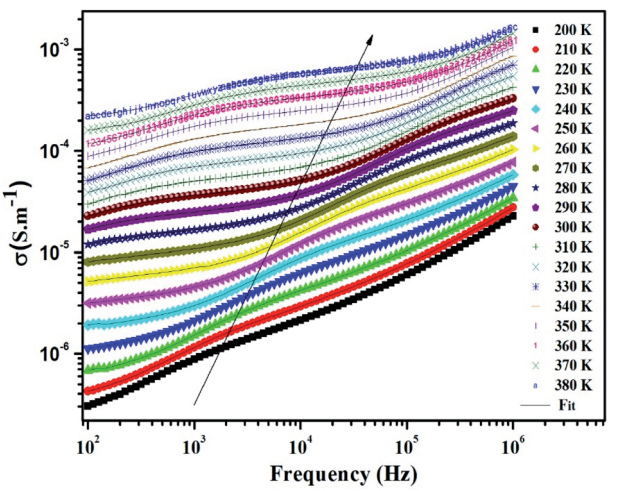

Fig. 7 Frequency variation of conductivity at selected temperatures of $LiMn_{0.5}Fe_2O_4$.

behavior by the leap of the localized load carrier, where the hole jumps between Mn^{3+} and Mn^{2+} cation and the electron hops between Fe^{2+} and Fe^{3+} ion. The semiconductor nature indicates that these compounds can be promising in certain applications such as optoelectronics, photodetectors, and photovoltaics.[7,32]

At higher frequencies (>10^4 Hz), the conductivity increases with increasing frequency. This can be explained by the important contribution of the charge carrier and the jumping mechanism.[54] This region is attributed to the alternating conductivity (σ_{ac}). Generally, the electrical conductivity behavior obeys the common universal power law, as reported by Jonscher.[54]

$$\sigma_T = \sigma_{dc} + \sigma_{ac} = \sigma_{dc} + A\omega^s \quad (15)$$

where σ_{dc} denotes the static component of the conductivity (at low-frequency value), ω is the angular frequency, and A is the pre-exponential factor. The exponent s represents the degree of interaction between the mobile ions and the environments around them. It is a positive exponent less than unity ($0 < s < 1$).

Fig. 8 illustrates the logarithmic variation of the conductivity σ_{dc} *versus* the inverse of the temperature. This curve can be described according to the Arrhenius relation.[55]

$$\sigma_{dc} = \sigma_0 \exp\left(-\frac{E_a'}{k_B T}\right) \quad (16)$$

σ_0 is the pre-exponential factor, E_a' is the minimum amount of energy to activate a process, and k_B is Boltzmann's constant with a defined value of 8.625×10^{-5} eV K^{-1}.

We acquire three linear regions in the curve, which has thermal activation, where the activation energies are 370 meV, 255 meV, and 199 meV for the first, second, and third region, respectively. These values are close to the obtained from $\ln(f_{max})$ *vs.* $1000/T$ (Fig. 6) with a slight variation, possibly due to the values of frequency taken from the different spectra. This proposes that during relaxation and conduction processes, the mobile charge carriers need to overcome roughly the same energy barrier.[34]

The experimental curves of conductivity are simulated using eqn (15) to deduce the value of exponent s at different temperatures to determine a suitable conduction mechanism in our material.

Many researchers have proposed several models to explain the behavior of the exponent s such as the correlated barrier hopping CBH model, where the charge carriers hop between sites above the potential barrier between them, as introduced by Elliot,[56] similar to the quantum mechanical tunneling mechanism (QMT) by Austin-Mott.[57] Further, we find the overlapping large-polaron tunneling (OLPT) and non-overlapping small polaron tunneling (NSPT). The last three models (QMT, NSPT, and OLPT) are related to the carrier motion, which occurs through the tunnel effect between two localized states near the Fermi level.[58]

Fig. 9 exhibits that s decreases with increasing temperature in two regions, namely, 200–270 K and 340–380 K. Such a behavior is consistent with correlated barrier hopping,[59] whereas the exponent s presents a tendency to increase with increasing temperature in the intermediate region [280–330 K]. Therefore, the NSPT model is an adequate mechanism to characterize the electrical conduction.

For the CBH model, the exponent s is given by[60]

$$s = 1 - \frac{6k_B T}{W_H + k_B T \ln(\omega\tau_0)} \quad (17)$$

where W_H signifies the potential barrier (the energy must be required the polaron to cross the barrier) and τ_0 means the relaxation time. In the case of fairly large values of $\frac{W_H}{k_B T}$, s can be written as follows.[60]

$$s = 1 - \frac{6k_B T}{W_H} \quad (18)$$

We can extract the value of the potential barrier W_H from the slopes of the temperature evolution curve of (1 s). In the range of 200–270 K and 340–380 K, it is equal to 236 and 178 meV, respectively (Fig. 9).

Fig. 10 displays the temperature dependence of the AC conductivity at different frequencies. For each fixed frequency,

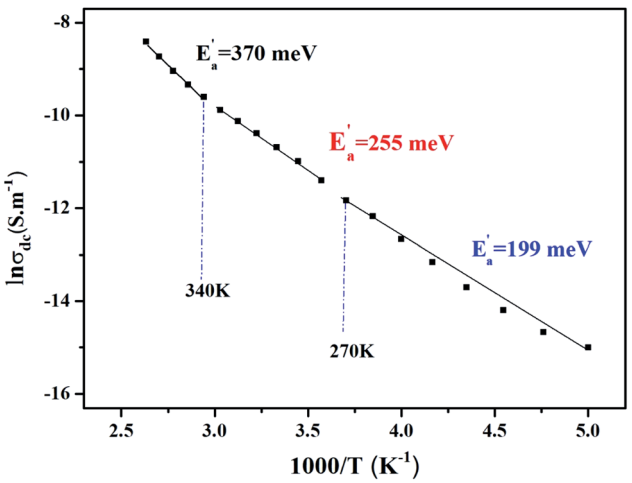

Fig. 8 Variation of ln (σ_{dc}) *vs.* $1000/T$.

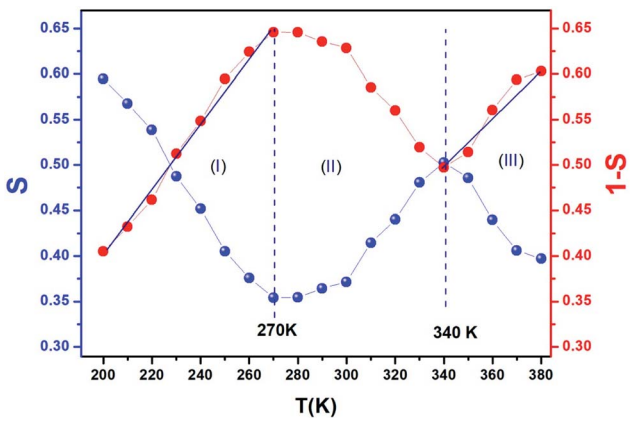

Fig. 9 Thermal variation of exponent "s" and "$1-s$" of $LiMn_{0.5}Fe_2O_4$.

$\ln(\sigma_{ac})$ decreases with rising of the reverse of temperature, showing three linear upright lines with different inclines (regions I, II, and III). The values of the activation energies extracted from the fit of data in the figure are summarized in Table 4. It is plain to see that E_a decreases with the increase in the frequencies at various temperature ranges. This can be associated with the increase in the applied field frequency, which enhances the electronic jump between localized states.[61] To put forward, we can affirm that the mobility of charge carriers in the compound is supplied by the hopping conduction mechanism.[61]

The high annealing temperature (1100 °C) causes the vibration of metal ions present in the ferrite (Li, Mn, Fe). The lithium-oxygen bonds (Li–O) are affected by the fine fraction due to the relatively smaller weight of lithium.[7] The breaking of some lithium and oxygen bonds enriches the release of electron and avails free lithium ions.[62] Thus, Mn, Fe, O, and mobile Li ions participate in conduction but in varying proportions.

In order to acquire more valuable information on the conduction process and to explore the dynamics of load carriers in $LiMn_{0.5}Fe_2O_4$, we were interested in the application of the Ghosh scaling model[63] and the Summerfield scaling model.[64] To obtain an appropriate scaling mechanism, the conductivity spectra at different temperatures exhibit a single universal master curve.[60] Evidently, we presume that the conductivity follows the time–temperature superposition principle (TTSP).[65] The plot of the conductivity isotherms is scaled according to the below general expression.[65]

$$\frac{\sigma_{ac}}{\sigma_{dc}} = F\left(\frac{\upsilon}{\upsilon_s}\right) \tag{19}$$

In the abovementioned expression, F denotes the temperature-independent function, σ_{dc} is the direct current conductivity, and υ_s indicates the scaling frequency. In the event of Ghosh scaling, υ_s is equal to υ_H, where υ_H is the hopping frequency obtained from the equation.[66]

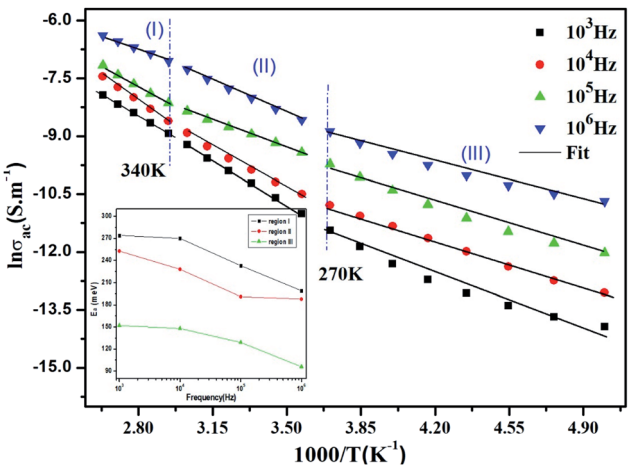

Fig. 10 Plots of $\ln \sigma_{ac}$ *vs.* $1000/T$ at different frequencies and the variation of the activation energy with the chosen frequencies inset.

Table 4 The activation energy values at chosen frequencies

Frequency (Hz)		10^3	10^4	10^5	10^6
E_a (meV)	Region (I)	274	270	233	199
	Region (II)	253	228	191	188
	Region (III)	152	148	129	96

$$\upsilon_H = \left(\frac{\sigma_{dc}}{A}\right)^{\frac{1}{s}} \tag{20}$$

However, in the case of Summerfield scaling, $\upsilon_s = \sigma_{dc}T$. In the present section, we study the scaling ac conductivity plot for $LiMn_{0.5}Fe_2O_4$ as a function of the latter scaling parameters. Fig. 11a exhibits the Ghosh scaling model and Fig. 11b shows the Summerfield scaling model at the investigated temperature range from 200 to 380 K for our prepared compound. It is observed that the curve shapes did not collapse into a unique master curve. This implies that the conductivity isotherms do not obey the time-temperature superposition principle (TTSP). The failure of the Summerfield scaling approach is due to the dissimilar dynamics of the load carriers over the studied frequency and temperature ranges.[67] Such behaviors are possibly related to an alteration in the load carrier density or change in the accessible pathways for the conduction transport number with temperature.[67] The presence of various available pathways ensures the conduction transport.[67]

The Summerfield scaling deviations are corrected using the Random Barrier Model (RBM). Then, the master curves should be restructured and introduced by modifying the scaling frequency axis υ_s by $\sigma_{dc}T\left(\frac{T}{T_0}\right)^{\alpha}$, as depicted in Fig. 11c, where T_0 is the initial temperature and α reveals the potency of the interaction force of the coulombic interaction between the charge carriers. The figure shows that all the isotherm conductivity curves are superposed into a master curve. The corrected scaling process holds in the case of the synthesized sample with a positive exponent α.

The value of α depends on the temperature (inset Fig. 11c), indicating the existence of coulombic interactions between the load carriers.[68]

It is well known that the temperature coefficient of resistivity (TCR) is important, especially for device performances for ameliorating the sensitivity of uncooled infrared bolometers.[34] We checked if our sample can be useful for these device applications. The TCR was calculated by the following equation.[69]

$$\mathrm{TCR}(\%) = \left[\frac{1}{\rho}\left[\frac{d\rho}{dT}\right]\right] \times 100 \tag{21}$$

where $\rho = \frac{1}{\sigma_{dc}}$ and T refer to the resistivity and temperature, respectively. We plotted the variation of TCR *versus* temperature in Fig. 12 in order to determine the TCR factor. As it is clear in Fig. 12, the value reaches about $-5.5(\%)$ K^{-1}. Comparing the obtained value of TCR to other values collected from previous works, we can consider $LiMn_{0.5}Fe_2O_4$ as a good candidate for

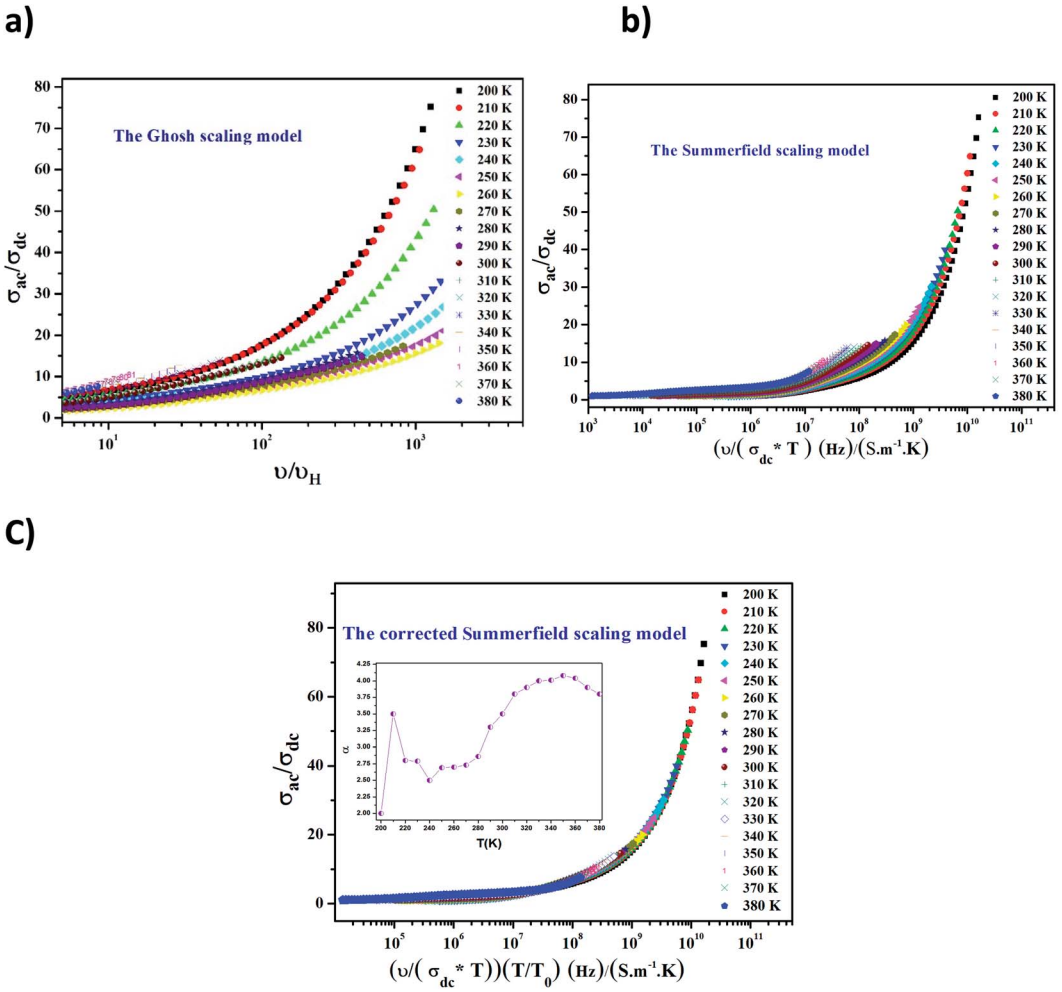

Fig. 11 The Ghosh scaling (a), conductivity spectra plotted at different temperatures according to Summerfield scaling (b), corrected Summerfield scaling, and the temperature dependence of the exponent α (c).

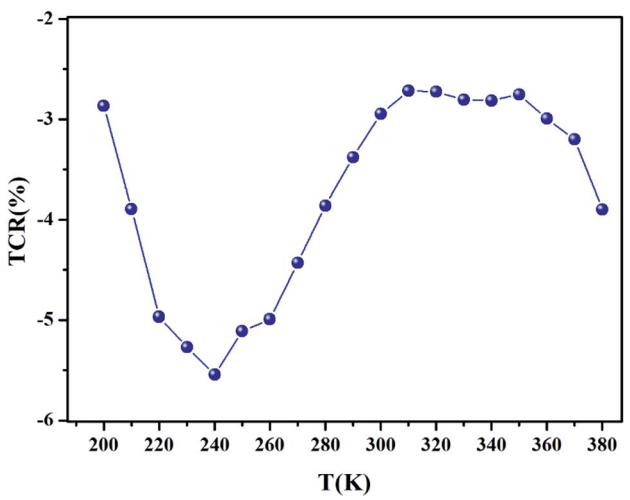

Fig. 12 Temperature dependence of TCR (%) parameter for $LiMn_{0.5}Fe_2O_4$.

detecting infrared radiations and infrared bolometric applications.[70,71]

4. Conclusion

In view of renewed interest in multifunctional molecular systems, we examine the structural, morphology, and electrical properties of $LiMn_{0.5}Fe_2O_4$ prepared *via* the solid state. The highly crystalline quality of the obtained particles is confirmed by the XRD measurements. The title compound crystallizes in the cubic phase of the $Fd\bar{3}m$ space group, and no secondary phase is noted. Furthermore, EDX proves a homogeneous distribution of iron and manganese cations. A detailed analysis of the impedance data reveals the grain and the grain boundary contribution, where the conductivity measurement confirms the semiconducting nature of the sample and examines the charge carrier transport mechanisms. The semiconductor nature indicates that the studied material can be promising in various applications such as optoelectronics, photodetectors, and photovoltaics. Two conduction mechanisms characterize

the electrical behavior, which are the correlated barrier hopping model (CBH) and the non-overlapping small polaron tunneling (NSPT). Also, the high value of the resistance coefficient TCR (-5.5 (%) K^{-1}) makes the material a good candidate for detecting infrared radiations and infrared bolometric applications.

This finding reveals that $LiMn_{0.5}Fe_2O_4$ was prepared and characterized as a multifunctional material, which opens up new possibilities for developing molecular functional materials, which is desirable to meet the rapidly increasing demand for technological applications. Nevertheless, the magnetic and dielectric properties as a function of temperature in $LiMn_{0.5}Fe_2O_4$ are perspectives in order to complete this work.

Conflicts of interest

Authors declare that they have no conflict of interest or personal relationships that could have appeared to influence the work reported in this paper.

References

1 N. Amri, J. Massoudi, K. Nouri, M. Triki, E. Dhahri and L. Bessais, *RSC Adv.*, 2021, **11**, 13256.
2 J. Massoudi, O. Messaoudi, S. Gharbi, T. Mnasri, E. Dhahri, K. Khirouni, E. Hlil, L. Alfhaid, L. Manai and A. Azhary, *J. Phys. Chem. C*, 2022, **126**, 2857.
3 R. Lahouli, J. Massoudi, M. Smari, H. Rahmouni, K. Khirouni, E. Dhahri and L. Bessais, *RSC Adv.*, 2019, **9**, 19949.
4 E. Morán, M. C. Blesa, M. E. Medina, J. D. Tornero, N. Menéndez and U. Amador, *Inorg. Chem.*, 2002, **41**, 5961.
5 M. Junaid, M. A. Khan, Z. M. Hashmi, G. Nasar, N. A. Kattan and A. Laref, *J. Mol. Struct.*, 2020, **1221**, 128859.
6 N. Singh, A. Agarwal and S. Sanghi, *Curr. Appl. Phys.*, 2011, **11**, 783.
7 D. Bouokkeze, J. Massoudi, W. Hzez, M. Smari, A. Bougoffa, K. Khirouni, E. Dhahri and L. Bessais, *RSC Adv.*, 2019, **9**, 40940.
8 A. A. Yousif, M. E. Elzain, S. A. Mazen, H. H. Sutherland, M. H. Abdalla and S. F. Mansour, *J. Condens. Matter Phys*, 1994, **6**, 5717.
9 D. Ravinder and P. Vijaya Bhasker Reddy, *Mater. Lett.*, 2003, **57**, 4344.
10 A. Manzoor, M. A. Khan, A. Shahzad, T. I. Al-Muhimeed, A. A. Al Obaid, H. Al balawi, A. M. Afzal, M. Kashif, S. Tahir and T. Munir, *Ceram. Int.*, 2021, **4**, 22662.
11 J. Jing, L. Liangchao and X. Feng, *J. Rare Earths*, 2007, **25**, 79.
12 G. Aravind, M. Raghasudha, D. Ravinder, M. M. Raja, S. S. Meena, P. Bhatt and M. Hashim, *Ceram. Int.*, 2016, **42**, 2941.
13 M. Srivastava, S. K. Alla, S. S. Meena, N. Gupta, R. K. Mandal and N. K. Prasad, *Ceram. Int.*, 2019, **45**, 12028.
14 S. H. Chen, S. C. Chang and L. N. Lin, *J. Magn. Magn. Mater.*, 2000, **209**, 193.
15 S. T. Assar, H. F. Abosheiasha and M. K. El Nimr, *J. Magn. Magn. Mater.*, 2014, **350**, 12.
16 V. Verma, M. Abdullah dar, V. Pandey, A. Singh, S. Annapoorni and R. K. Kotnala, *Mater. Chem. Phys.*, 2010, **122**, 133.
17 S. C. Watawe, U. A. Bamne, S. P. Gonbare and R. B. Tangsali, *Mater. Chem. Phys.*, 2007, **103**, 323.
18 N. Kumar, R. K. Singh and H. K. Satyapal, *J. Mater. Sci.: Mater. Electron.*, 2020, **31**, 9231.
19 V. Verma, M. A. Dar, V. Pandey, A. Singh, S. Annapoorni and R. K. Kotnala, *Mater. Chem. Phys.*, 2010, **122**, 133.
20 Z. K. Heiba, M. M. S. Sanad and M. B. Mohamed, *Solid State Ionics*, 2019, **341**, 115042.
21 N. Gupta, S. C. Kashyap and D. C. Dube, *Phys. Status Solidi A*, 2007, **204**, 2441.
22 P. P. Hankare, R. P. Patil, U. B. Sankpal, S. D. Jadhav, P. D. Lokhande, K. M. Jadhav and R. Sasikala, *J. Solid State Chem.*, 2009, **182**, 3217.
23 T. N. Pham, T. Q. Huy and A. T. Le, *RSC Adv.*, 2020, **10**, 31622.
24 S. Bellad and B. Chougule, *Mater. Chem. Phys.*, 2000, **66**, 58.
25 S. C. Watawe, U. A. Bamne, S. P. Gonbare and R. B. Tangsali, *Mater. Chem. Phys.*, 2007, **103**, 323.
26 J. Massoudi, D. Bouekkeze, A. Bougoffa, K. Khirouni, E. Dhahri and L. Bessais, *Adv. Powder Technol.*, 2020, **31**, 4714.
27 L. Li, X. Zhang, R. Chen, T. Zhao, J. Lu, F. Wu and K. Amine, *J. Power Sources*, 2014, **249**, 28.
28 J. Massoudi, M. Smari, K. Khirouni, E. Dhahri and L. Bessais, *J. Magn. Magn. Mater.*, 2021, **528**, 167806.
29 G. R. Gajula, L. R. Buddiga, K. N. Chidambara Kumar, C. Arun Kumar and M. Dasari, *J. Sci.: Adv. Mater. Devices*, 2018, **3**, 230.
30 R. N. Bhowmik and G. Vijayasri, *Int. J. Appl. Phys.*, 2013, **114**, 223701.
31 A. Agajanian, *IEEE Trans. Magn.*, 1970, **6**, 90.
32 H. M. Rietveld, *J. Appl. Crystallogr.*, 1969, **2**, 65.
33 M. Kurian, S. Thankachan, D. S. Nair, E. K. Aswathy, A. Babu, A. Thomas and B. K. KT, *J. Adv. Ceram.*, 2015, **4**, 199.
34 A. Hadded, J. Massoudi, E. Dhahri, K. Khirouni and B. F. O. Costa, *RSC Adv.*, 2020, **10**, 1042542.
35 M. Bouzayen, R. Dhahri, A. Benali, S. Chaabouni, K. Khirouni and B. F. O. Costa, *Chem. Phys. Lett.*, 2020, **741**, 137106.
36 D. Zákutná, J. Vlček, P. Fitl, K. Nemkovski, D. Honecker, D. Nižňanský and S. Disch, *Phys. Rev. B*, 2018, **98**, 064407.
37 N. Tawichai, K. Sutjarittangtham, T. Tunkasiri, K. Pengpat, G. Rujijanagul and J. Wang, *Ceram. Int.*, 2013, **39**, 145.
38 H. Rahmouni, M. Smari, B. Cherif, E. Dhahri and K. Khirouni, *Dalton Trans.*, 2015, **44**, 10457.
39 P. Córdoba-Torres, T. J. Mesquita, O. Devos, B. Tribollet, V. Roche and R. P. Nogueira, *Electrochim. Acta*, 2012, **72**, 172.
40 A. B. J. Kharrat, N. Moutia, K. Khirouni and W. Boujelben, *Mater. Res. Bull.*, 2018, **105**, 75.
41 Kh. Ben Brahim, M. Ben gzaiel, A. Oueslati and M. Gargouri, *RSC Adv.*, 2018, **8**, 40676.
42 M. Shah, M. Nadeem, M. Idrees, M. Atif and M. J. Akhtar, *J. Magn. Magn. Mater.*, 2013, **332**, 61.
43 F. S. H. Abu-Samaha and M. I. M. Ismail, *Mater. Sci. Semicond. Process.*, 2014, **19**, 50.

44 F. B. Abdallah, A. Ben ali, M. Triki, E. Dhahri, M. P. F. Graça and M. A. Valente, *Superlattices Microstruct.*, 2018, **117**, 260.
45 W. B. Soltan, S. Nasri, M. S. Lassoued and S. Ammar, *J. Mater. Sci.: Mater. Electron.*, 2017, **28**, 6356.
46 A. Rouahi, A. Kahouli, F. Challali, M. P. Besland, C. Vallée, B. Yangui, S. Salimy and A. Sylvestre, *J. Phys. D: Appl. Phys.*, 2013, **46**, 65308.
47 F. I. H. Rhouma, A. Dhahri, N. Farhat, J. Dhahri and K. Khirouni, *EPJ Web Conf.*, 2012, **29**, 23.
48 S. Chatterjee, P. K. Mahapatra, R. N. P. Choudhary and A. K. Thakur, *Phys. Status Solidi A*, 2004, **201**, 588.
49 L, K. Kumari, K. Prasad and R. N. P. Choudhary, *J. Alloys Compd.*, 2008, **453**, 325.
50 K. S. Cole and R. H. Cole, *J. Chem. Phys.*, 1941, **9**, 341.
51 A. Bougoffa, J. Massoudi, M. Smari, E. Dhahri, K. Khirouni and L. Bessais, *J. Mater. Sci.: Mater. Electron.*, 2019, **30**, 21018.
52 C. Bharti and T. P. Sinha, *Phys. Rev. B*, 2011, **406**, 1827.
53 A. Dutta, C. Bharti and T. P. Sinha, *Phys. Rev. B*, 2008, **403**, 3389.
54 S. Şenkul, R. Taş, S. Sönmezoğlu and M. Can, *Int. J. Polym. Anal. Charact.*, 2012, **17**, 257.
55 R. Hanen, A. Mleiki, H. Rahmouni, N. Guermazi, K. Khirouni and A. cheikhrouhou, *J. Mater. Sci.: Mater. Electron.*, 2020, **31**, 16830.
56 S. R. Elliott, *Adv. Phys.*, 1987, **36**, 135.
57 N. F. Mott, *Philos. Mag. B*, 1980, **42**, 327.
58 M. Ennefati, B. Louati, K. Guidara, M. Rasheed and R. Barillé, *J. Mater. Sci.: Mater. Electron.*, 2018, **29**, 171.
59 M. Megdiche, C. Perrin-Pellegrino and M. Gargouri, *J. Alloys Compd.*, 2014, **584**, 209.
60 P. K. Singh, S. K. Sharma, S. K. Tripathi and D. K. Dwivedi, *Results Phys.*, 2019, **12**, 223.
61 M. Okutan, E. Basaran, H. I. Bakan and F. Yakuphanoglu, *Phys. Rev. B*, 2005, **364**, 300.
62 C. M. Julien and M. A. Camacho-Lopez, *Mater. Sci. Eng., B*, 2004, **108**, 179.
63 A. Ghosh and A. Pan, *Phys. Rev. Lett.*, 2000, **84**, 2188.
64 S. Summerfield, *Philos. Mag. Part B*, 1985, **52**, 9.
65 Y. Moualhi, H. Rahmouni and K. Khirouni, *Phys. B*, 2021, **616**, 413129.
66 S. Singh, P. A Jha, S. Varma and P. Singh, *J. Alloys Compd.*, 2017, **704**, 707.
67 T. Dabbebi, S. Hcini, B. Alzahrani, H. Rahmouni, E. Dhahri, H. Al Robei and M. L. Bouazizi, *J. Mater. Sci.: Mater. Electron.*, 2021, **56**, 1.
68 Y. Moualhi, R. M'nassri, M. M. Nofal, H. Rahmouni, A. Selmi, M. Gassoumi, N. Chniba-Boudjada, K. Khirouni and A. Cheikhrouhou, *J. Mater. Sci.: Mater. Electron.*, 2020, **31**, 21046.
69 H. Chouaya, M. Smari, I. Walha, E. Dhahri, M. P. F. Graça and M. A. Valente, *J. Magn. Magn. Mater.*, 2018, **451**, 344.
70 X. Liu, Y. Z. Yan, Q. M. Chen, H. Zhang, M. G. Cao, S. C. Zhang and P. X. Zhang, *Appl. Surf. Sci.*, 2013, **283**, 851.
71 J. Massoudi, M. Smari, K. Nouri, E. Dhahri, K. Khirouni, S. Bertaina and L. Bessais, *RSC Adv.*, 2020, **10**, 34556.